Synergetic effects of dual-beam implantation on the microstructural development in silicon

F. Fortuna,[1] V. A. Borodin,[2] M.-O. Ruault,[1] E. Oliviero,[1] and M. A. Kirk[3]
[1]*CSNSM, bâtiment 108, 91405 Orsay Campus, France*
[2]*NRC Kurchatov Institute, Kurchatov Square, 1, 123182 Moscow, Russia*
[3]*Materials Science Division, Argonne National Laboratory, Argonne, Illinois 60439, USA*
(Received 22 July 2011; revised manuscript received 26 September 2011; published 28 October 2011)

We report a synergy effect on the microstructural development of silicon specimens as a result of dual-beam high temperature irradiation/implantation. *In situ* transmission electron microscopy experiments using two different experimental setups have been used, where the primary 50 keV Co^+ ion implantation beam was supplemented with either a 300 keV electron beam or a 500 keV Si^+ ion beam. In both cases, the secondary beam intensity was such that both beams created comparable overall primary damage. Completely different microstructural response has been found in these two cases. An intensive electron irradiation was found to sharply accelerate the evolution of dislocation structure, only weakly affecting the disilicide kinetics. On the contrary, the Si ion beam weakly affected the kinetics of either dislocation loops or coherent $CoSi_2$ precipitates, but drastically increased the number density of thermodynamically unstable semicoherent precipitates. Possible microstructural reasons for the observed effects and the implications for both dislocation loop and cobalt disilicide nucleation mechanisms in high-temperature implanted TEM samples are discussed and supported by detailed molecular dynamics calculations of annealing of cascade remnants produced by the energetic silicon recoils.

DOI: 10.1103/PhysRevB.84.144118 PACS number(s): 61.80.−x, 68.37.Lp, 68.55.Ln, 81.40.Wx

I. INTRODUCTION

The growth of new solid phases in various materials can be efficiently achieved by ion implantation. Using various ions beams and appropriate implantation conditions, it is possible to synthesize even such phases that cannot be created in other ways. The nucleation of a new phase involves a complex interplay of multiple processes prompted by implantation. Saturating a substrate with implant atoms, implantation causes at the same time severe radiation damage in the form of self-interstitial atoms, vacancies, and small defect clusters. Interaction between implant atoms and radiation damage is typically synergetic; the behavior of both implant atoms and radiation defects during implantation can be completely different from their behavior in out-of-beam conditions. This synergy, in turn, affects the kinetics and outcome of new phase precipitation. To efficiently control the radiation induced synthesis (RIS), the mechanisms of synergetic action of implanted ions and radiation damage have to be properly understood.

In the conventional RIS setup, it is hard to separate contributions of implant atoms and radiation damage because the damage production is predetermined by the implantation regime. However, such separation can be achieved using dual-beam experiments. By modifying the intensity of a secondary beam, one can gain deeper insights on the radiation damage effects on the implant diffusion and precipitation. By applying different secondary beams, not only the damage production efficiency can be changed, but also the damage mode can be modified. For example, a self-ion secondary beam increases the point defect generation rate in the cascade mode, whereas a sufficiently energetic electron beam creates radiation damage in a simple form of freely migrating vacancies and self-interstitials.

The dual-beam implantation is not the only condition for understanding the interplay of different microstructural features during RIS. It is equally important to detect the differences caused by the application of a secondary beam, using proper visualization means and model systems, where the effect of the second beam can be identified. For second phase precipitation, the most detailed information about particle nucleation and growth is given by transmission electron microscopy (TEM). Ideally, a facility to study synergetic effects of implant supply and radiation damage production would perform dual-beam implantation directly in the column of TEM. Where the second beam of fast electrons is of interest, one can use a single beam online with sufficiently powerful electron microscope (e.g. no less that 300 kV for silicon substrates). Such facilities are rare, but existing. Here, we demonstrate an application of both types of facilities—JANNuS-Orsay (CSNSM, France) and IVEM (ANL, US)—to the investigation of dual-beam synergy effects on a model system.

The model system considered here is cobalt-implanted silicon. The cobalt implantation into silicon with the aim of creating cobalt disilicide ($CoSi_2$) precipitates or thin layers is common to microelectronic applications exploiting such properties of metal silicides as high electric conductivity and high-temperature stability.[1] A special advantage for the current study is the fact that the precipitation of $CoSi_2$ is very sensitive to the experimental conditions. A direct high-temperature Co implantation results in qualitatively different precipitate populations than a sequence of low-temperature implantation and subsequent high-temperature annealing.[2–4] Our earlier research[4,5] suggests that this effect is the direct consequence of radiation damage intervention into the kinetics of Co precipitation.

In order to compare the dual-beam implantation results with those acquired earlier for single-beam implantation, we used here essentially the same primary beam of cobalt ions. However, now the Co beam is supplemented with secondary beams of strongly different type, namely high-energy electron beam or Si ion beam. The paper discusses the manifestation and possible reasons for the observed synergetic dual-beam

effects on microstructure evolution and $CoSi_2$ precipitation during high-temperature ion implantation.

II. EXPERIMENTAL TECHNIQUES

In situ experiments under dual-beam irradiation require, first of all, the availability of relevant equipment. In order to use the advantage of various secondary beam types, we had to use two experimental facilities (IVEM in Argonne and JANNuS in Orsay), as described below. However, the silicon samples from the same batch were studied, and similar experiment conditions were applied. Namely, both experiments were performed at 650 °C on low-doped (6×10^{12} P/cm^3) float-zone Si samples with a (100) basic plane orientation. Discs of 3 mm in diameter were chemically thinned for transmission electron microscopy (TEM).

In both experiments, the sample area covered by Co implantation beam was larger than the spot covered by a secondary (either electron or Si) beam. Thus, each sample contained a referent exposed to a single Co beam. Correspondingly, the effects of single and double beams could be compared on two areas from the same sample: one that has seen only the Co beam and another one that has seen both beams.

A detailed description of experimental facilities and facility-relevant conditions is given below.

A. IVEM

The simultaneous *in situ* implantation and electron irradiation requires a sufficiently powerful (at least 300 keV electron energy and 0.6 μA current) electron microscope on line with the implantation beam. These requirements are met at IVEM facility in ANL, where a modified Hitachi (H-9000NAR) intermediate-voltage electron microscope is interfaced with an ion implanter (650 kV NEC). The angle between incident electron and ion beam is 30°. For complete details of the facility see Ref. 6.

In the current experiment, the sample was tilted (around 20°) so that the electron beam was perpendicular to a (114) plane, which is used to observe the B-type $CoSi_2$ precipitates. In this configuration, the Co ion beam was at ∼8° off the basal (100) plane of the sample, like in the previous experiments reported in Ref. 4. The following combinations of irradiation/implantation parameters were applied: (i) 50 keV Co^+ beam with ion fluxes of 1.0 or 2.5×10^{11} ions/cm^2/s covering the whole area of the sample, and (ii) 300 keV electron beam with the fluxes of 1.0 or 2.0×10^{19} e$^-$/cm^2/s on a small area of the sample (typically a spot of ∼1–1.5 μm in diameter). The total ion fluences for different combinations of ion and electron beam currents varied in the range of $(4.5–8) \times 10^{14}$ Co^+/cm^2. In each experimental run, the Co^+ beam was switched off at several intermediate doses in order to investigate the developed microstructure, while the electron energy was simultaneously lowered down to 150 keV; that is below the displacement energy threshold. In parallel, the sample heating was switched off.

In order to get a better understanding of the studied phenomena, also a 300 keV single-beam electron irradiation of a separate Si sample up to a fluence of 10^{23} electrons/cm^2 was performed in the same conditions as for the dual-beam experiment.

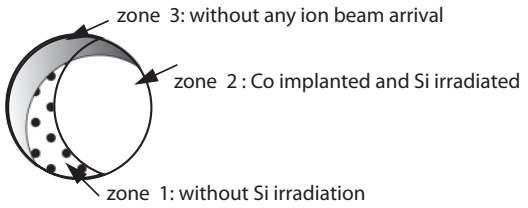

FIG. 1. A scheme of irradiated/implanted zones on the sample, taking into account the shadows due to the sample holder.

B. JANNuS

The possibility for the combination of Co implantation and Si irradiation has appeared recently after the launch of the Joint Accelerators for Nano-science and Nuclear Simulation at Orsay (JANNuS-Orsay) platform. The facility consists of two accelerators (a 190-kV ion implanter IRMA and a 2-MV Tandem/Van de Graff accelerator ARAMIS) coupled to a 200-kV TEM (Tecnai G_2 20). It is designed to supply a large range of ion irradiation and implantation conditions, allowing *in situ* TEM with single- or dual-beam combinations. Detailed description of the facility can be found in Ref. 7. In these experiments, the electron acceleration voltage of the TEM was chosen at the level of 150 kV in order to avoid unintentional defect creation in investigated samples.

In the current experiments, dual-beam irradiation was applied. The first beam was 50-keV Co^+ with a flux of 3.3×10^{11}ions/cm^2/s up to a fluence of 8×10^{14}ions/cm^2. The second beam was 500-keV Si^+ with a flux of 10^{12}ions/cm^2/s. The Si^+ beam was switched on during the Co implantation, resulting in a total silicon fluence of 2.4×10^{15}ions/cm^2. The sample holder was double tilted. Both beams were inclined with respect to the sample normal, with inclination angles of 63° and 49° for cobalt and silicon beams, respectively. The shadow due to the sample holder for each ion beam is illustrated in Fig. 1. The studied sample was positioned so that we could observe thin areas in zone 1 (without Si irradiation) as well as thin areas in zone 2 (under the dual ion beams).

In order to investigate the developed microstructure, both ion beams were switched off simultaneously at several intermediate doses, while the sample heating was cut off, like in IVEM experiments.

In order to obtain quantitative comparisons of microstructure characteristics (e.g. size and concentration), we performed the electron microscopy observations on areas with similar thickness, as evaluated from thickness fringes.

III. EXPERIMENTAL RESULTS AND THEIR ANALYSES

A. Experimental observations

1. Single-beam cobalt implantation

The results for single-beam Co implanted areas are essentially the same in both facilities (with allowance for inevitable variations in the rates of Co implantation and different samples) and follow the trend observed in our earlier experiments.[4] As in our earlier experiments, a simultaneous nucleation of

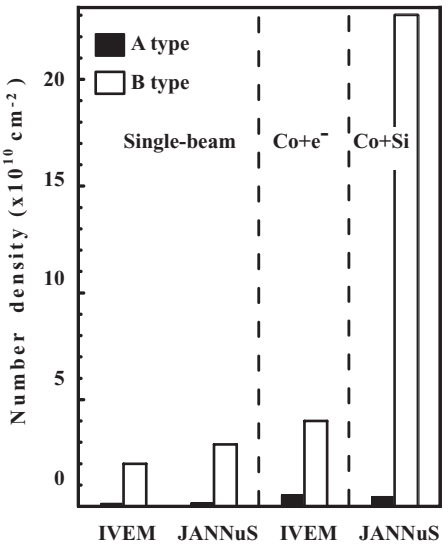

FIG. 2. The saturated number densities of $CoSi_2$ precipitates of A- and B-type in different experimental conditions.

two precipitate types is observed. Some precipitates (usually referred to as A-type) are octahedral, while the others (B-type) are platelet shaped. The number densities of both A- and B-type precipitates quickly reach saturation, and these saturated values are quite close in both facilities (see Fig. 2). The observable A-type precipitates appear in TEM in both cases at larger fluences than B-type. Typical precipitate mean sizes and the variances of size distributions, as exemplified in Fig. 3, are also very similar to the earlier observations.

The dislocation structure evolving during single-beam Co implantation also looks very similar for both IVEM and JANNuS. Summing up, the pure Co implantation on both facilities reproduces a consistent picture both qualitatively and quantitatively.

2. *Co-implantation of Co ions and fast electrons*

Firstly, no visible defects (dislocation loops, voids, etc.) were observed during the single-beam electron irradiation, even for a higher electron flux and a higher fluence than those reached in the dual-beam experiments described below.

In the dual-beam irradiation with Co ions and fast electrons, the most pronounced difference between the dual-beam and single-beam covered areas is the dislocation population

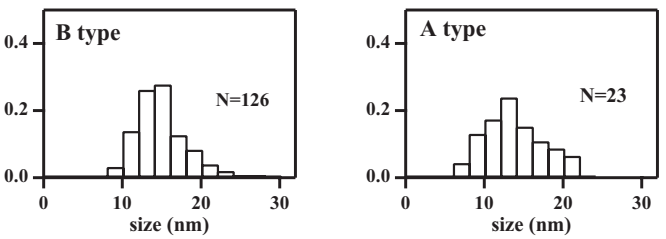

FIG. 3. B-type (left) and A-type (right) $CoSi_2$ precipitate size distributions at the Co ion fluence of $8 \times 10^{14}/cm^2$ (single-beam implanted area, JANNuS). Each histogram is normalized so that the area under the curve was equal to unity. The total numbers N of precipitates used for histogram creation are shown in figure legends.

kinetics. The loop kinetics were studied in detail in two runs, for ion/electron flux combinations (1.0×10^{11} $Co^+/cm^2/s$ + 2.0×10^{19} $e^-/cm^2/s$) or (2.5×10^{11} $Co^+/cm^2/s$ + 1.0×10^{19} $e^-/cm^2/s$). These will be referred to, respectively, as electron-biased and ion-biased regimes, since, as shown below in Sec. III B 1, the primary damage production in the first case is due more to electrons, while in the second one, it is due to ions. In both cases, big planar defects evolve in the irradiated samples. The exact nature of these defects is not easy to exactly verify, but their general appearance indicates them to be faulted dislocation loops.[8] The growth of dislocation loops is visibly accelerated in the electron-beam spot and in its close vicinity.

The effect is especially pronounced in the electron-biased regime, see Fig. 4. Already at 3×10^{14} Co^+/cm^2 (the first observation point) the biggest loop sizes reach hundreds of nanometers, see Figs. 4(a) and 4(b). Very long and narrow perfect dislocation loops are observed, which most probably result from intersection of some growing loops between themselves and with one or both sample surfaces. In the solely Co-implanted area, dislocation loop sizes are notably less, but the number density is quite high (Fig. 5). This dislocation structure did not change much with further irradiation [compare Figs. 4(a) and 4(b) with Figs. 4(c) and 4(d)], indicating that the dislocation kinetics is saturated already before the first observation point.

In the ion-biased regime, the dislocation loop kinetics could be followed in more detail. The snapshots of dislocation loop populations in the studied TEM sample within and well out of the electron beam spot are shown in Fig. 6. In order to provide a qualitative measure of the loop sizes, we use the largest length of the loop projections onto the (100) micrograph plane. It should not be forgotten that this is not necessarily the loop diameter, because the loops, especially the larger ones, are generally not circular, and the habit planes of the loops were not determined. The data on the loop number densities N_L and average projected loop lengths d_L at different Co ion fluences are given in Table I. The values of the loop number densities in Table I are estimates from calculated numbers of visible loops only, which underestimate the true number densities by at least a factor of two because the loop visibility depends on both the Burger's vectors (not determined here) and the **g** acting diffraction vector (220), as well as the loop position in the thin-layer TEM specimen.

As can be seen in Table I, both inside and outside of the electron-irradiated spot, the loop number density saturates at a certain level. Quite unexpectedly, the loop number density in the electron-irradiated spot is smaller by more than a factor of two. Correspondingly, the average projected length of visible dislocation loops inside the electron-irradiated spot notably exceeds that outside of it, Fig. 7. Figure 8 shows the histograms of visible loop distributions over sizes, normalized in each case so that the area under the curve equals unity. It can be seen that not only the average size of loops at a fixed dose is larger in the electron-irradiated spot, but also the size variance is notably broader.

In contrast to dislocation loops, the effect of electron beam on the disilicide precipitation kinetics is not spectacular. The qualitative data for both types of precipitates collected for the experiment with the highest electron flux are summarized in Table II. In the ion-biased regime, little effect of electrons on

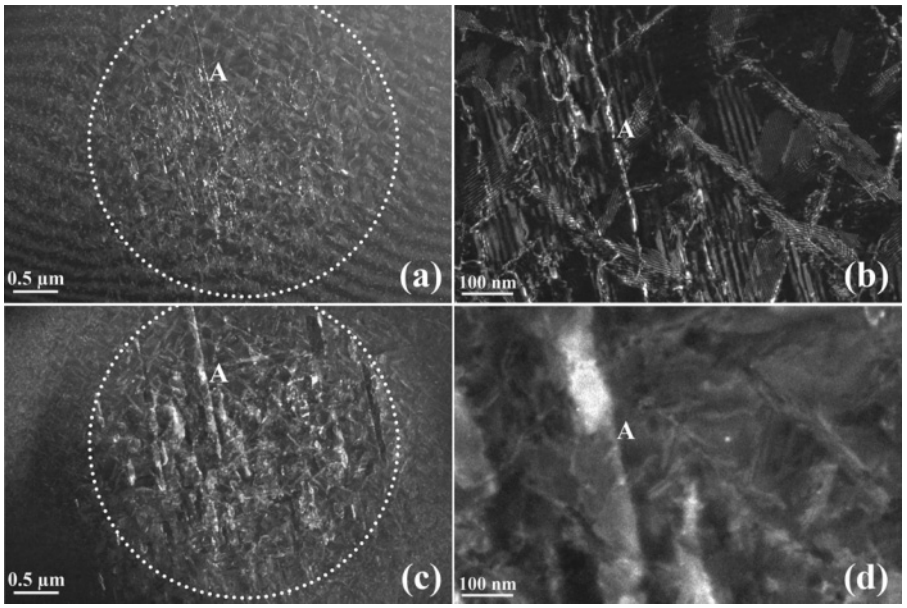

FIG. 4. Dark field TEM micrographs of the electron-irradiated spot region in the electron biased regime. (a) Top view of the area subject to both electron irradiation and Co implantation at Co ion fluence of $3 \times 10^{14}/\text{cm}^2$. (b) Zoom of (a) in the neighborhood of marker A. (c) Top view of the same area at Co ion fluence $6 \times 10^{14}/\text{cm}^2$. (d) Zoom of (c) in the neighborhood of marker A.

either number densities or sizes of A- and B-type precipitates is noticed. The increase of the electron flux up to 2.0×10^{19} $\text{e}^-/\text{cm}^2/\text{s}$ increases the number densities of both A- and B-type precipitates in the electron irradiated spot as compared to the outside area. A combination of the highest electron and ion fluences results in a more pronounced number density increase for A-type than for B-type, and the ratio of A/B number densities increases to ∼12%, as compared to ∼5% for the single-beam Co-implantation area. However, the ratio still remains in the standard range for *in situ* high-temperature implantation experiments (around 10%).[4] Variations of cluster sizes with the Co fluence reflect more or less the variations in the cluster number density, so that the total amount of Co in the clusters corresponds to the total number of implanted Co ions. The only exception is the combination of the highest electron

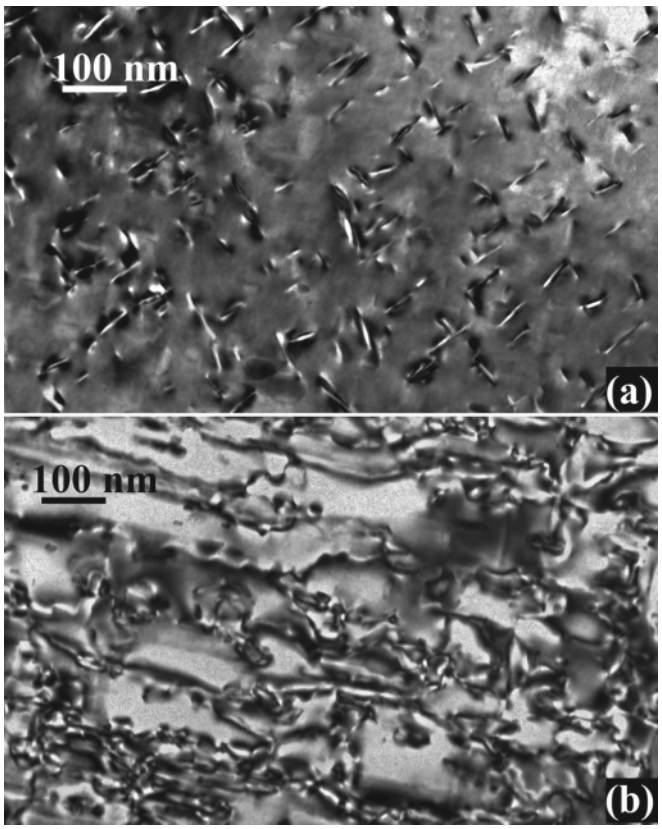

FIG. 5. Dynamical bright field TEM micrographs of the dislocation structure formed by Co ion fluence $4.5 \times 10^{14}/\text{cm}^2$ in electron biased regime: (a) In the region implanted with only Co ions and (b) inside the electron-irradiated spot.

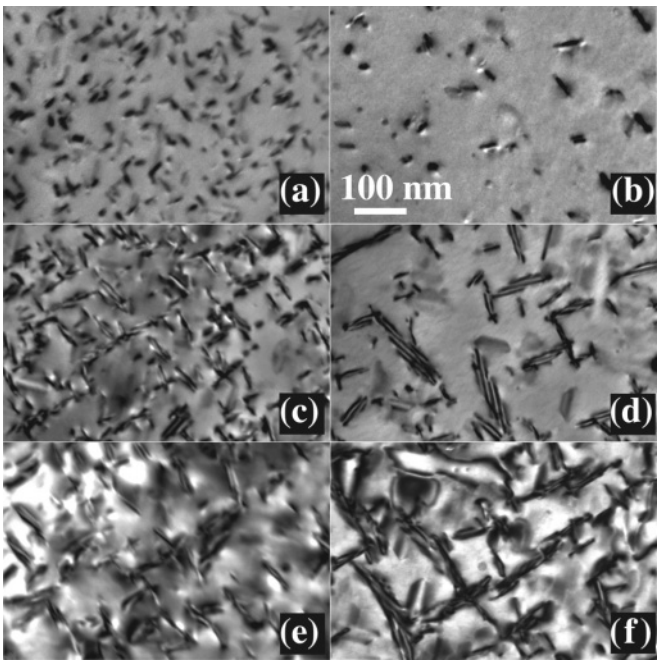

FIG. 6. Dislocation loop populations in the sample irradiated in the ion-biased regime outside (left column) and inside (right column) the electron-beam spot. All TEM micrographs are bright field and filmed on ⟨100⟩ zone axis. The fluences correspond to 2 (a) and (b), 5 (c) and (d) and 8×10^{14} Co^+/cm^2 (e) and (f).

TABLE I. Dislocation loop planar number densities N_L and average projected loop lengths d_L at different Co ion fluences for IVEM experiment in ion-biased regime.

Co fluence	$2 \times 10^{14}/\text{cm}^2$	$5 \times 10^{14}/\text{cm}^2$	$8 \times 10^{14}/\text{cm}^2$
	Single Co beam		
N_L ($10^{10}/\text{cm}^2$)	7	6	5
d_L (nm)	20	30	45
	Dual-beam Co+ e^-		
N_L ($10^{10}/\text{cm}^2$)	2	3	2
d_L (nm)	30	55	85

and ion fluences, where the estimated number of Co atoms in clusters is significantly (by several ten percent) lower than that implanted, indicating that a substantial Co fraction can be in substitutional positions or in invisible small Co-vacancy complexes.[4]

3. *Double-beam irradiation with Co and Si ions*

When Co implantation is coupled with Si irradiation, the outcome is completely different to Co/electron dual-beam irradiation. Silicon ion beam affects neither the dislocation structure nor the number density of A-type precipitates in any significant manner. The most impressive effect of the Si beam is the dramatic increase of B-type precipitate number density (Fig. 9), so that the A-type to B-type number density ratio falls down to ∼2%, Fig. 2. Correspondingly, at the same Co doses, the sizes of B-type precipitates (Fig. 10) are notably smaller than for single-beam Co implantation (Fig. 3). The qualitative data for both types of precipitates is summarized in Table III.

B. Data analysis

1. *The efficiency of point defect generation in dual-beam conditions*

In two-beam irradiation/implantation conditions, the rate of primary damage production can be considered as a sum of contributions from individual beams. For this reason, we start this section by estimating contributions to damage production for each beam involved in our experimental conditions. After

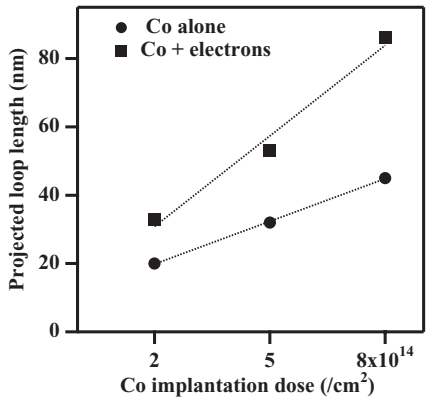

FIG. 7. The average projected loop length variation as a function of Co ion fluence. The data points are for the loops inside (squares) and outside (circles) of the electron-irradiated spot. The trend lines (dotted) are to guide the eye.

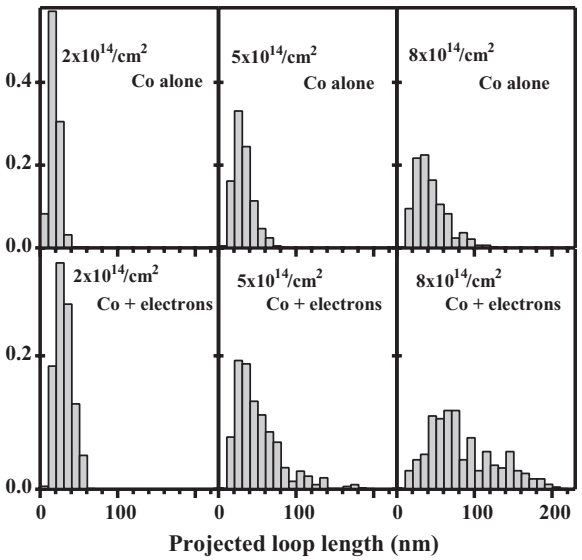

FIG. 8. The normalized distributions of observable loop projected length at different implantation doses inside and outside of the electron-irradiated spot.

that, the total amount of primary damage created by each particular beam is estimated, taking into account the modes of primary damage creation.

(a) The beam contributions in the IVEM experiment. The displacement production rate by Co ion beam, G_{Co}, can be estimated as

$$G_{\text{Co}} = g_{\text{Co}} \times \varphi_{\text{Co}} \times \Omega / h, \tag{1}$$

where g_{Co} is the average number of atomic displacements produced by a Co^+ projectile, φ_{Co} the ion flux, h the sample thickness, and $\Omega = 2 \times 10^{-23}$ cm^3 the atomic volume of Si in the bulk. The SRIM code[9]-based estimate with the full damage cascades calculation is $g_{\text{Co}} = 1.17 \times 10^3$/ion for the Co ion beam inclined at 8° to the sample surface. Taking here and below $h = 100$ nm, this gives $G_{\text{Co}} \approx 2.3 \times 10^{-4}$ and 6.7×10^{-4} dpa/s for the Co flux of 1.0 and 2.5×10^{11} ions/cm^2/s, respectively. The damage production is nonuniform over the sample thickness, Fig. 11, and the rate of displacement production in the displacement peak reaches $\approx 1.1 \times 10^{-3}$ dpa/s for the ion flux of 2.5×10^{11} ions/cm^2/s.

In contrast to Co ions, which are nearly completely captured in the TEM specimen, Fig. 11(a), 300-keV electrons easily pass through the specimen, creating damage uniformly over the sample thickness. The simplest estimate of the damage by fast electrons, G_e, involves the use of Mott damage creation cross section, which is estimated to be 48.8 barn for 300-keV electrons.[10] For the electron flux of $\varphi_e = 2 \times 10^{19}/\text{cm}^2/\text{s}$, this gives $G_e \approx 10^{-3}$ dpa/s.

We thus conclude that the total efficiencies of defect production for Co ions and 300-keV electrons are approximately the same in the experiment with the combination of the highest Co ion and electron fluxes. The decrease of either of two flux intensities introduces a bias in defect production, justifying the terminology applied above in Sec. III A 2.

(b) The beam contributions in the JANNuS experiment. In the case of the JANNuS experiment, Eq. (1) remains applicable for the estimation of the defect production rate by Co ion

TABLE II. $CoSi_2$ precipitate number densities, N_p, and mean sizes at different Co ion fluences for different combinations of ion/electron fluxes in IVEM experiment.

Co ion flux	Electron flux	$CoSi_2$	N_p	Mean size (nm) at Co fluences (Co^+/cm^2) of					
($10^{11}/cm^2/s$)	($10^{19}/cm^2/s$)	type	($10^{10}/cm^2$)	2×10^{14}	3×10^{14}	4.3×10^{14}	5×10^{14}	6×10^{14}	8×10^{14}
1.0	0.0	A	0.17			6			
1.0	0.0	B	1.6	14		20			
1.0	2.0	A	0.32			4			
1.0	2.0	B	3.0	10		15			
2.5	0.0	A	0.07	8			15		20
2.5	0.0	B	1.0	16			27		34
2.5	1.0	A	0.05	9			16		17
2.5	1.0	B	1.5	14			21		26
2.5	0.0	A	0.11					10	
2.5	0.0	B	2.0		13			16	
2.5	2.0	A	0.52					6	
2.5	2.0	B	4.0		8			10	

beam. The only difference is due to the fact that the beam is notably inclined with respect to the sample surface. As a result, both the ion and the displacement distributions are shifted toward the sample surface, Fig. 11. Correspondingly, though the average number of displacements ($g_{Co} \approx 1.1 \times 10^3$/ion) remains practically unchanged as compared to IVEM experiment, the damage peak value is higher. The average and the peak values of displacement generation rates obtained assuming the sample thickness of 100 nm are $G_{Co} \approx 8.3 \times 10^{-4}$ and 3.1×10^{-3} dpa/s, respectively.

The damage rate production by 500-keV Si ions, Fig. 11(b), is noticeably more uniform than that by Co ions because the absolute majority of projectiles transverse the sample (the ion capture probability is, according to SRIM, $\sim 5.2 \times 10^{-3}$/ion). The efficiency of displacement creation ($g_{Si} \approx 3.85 \times 10^2$/ion in a 100-nm-thick silicon layer) is less than for Co ions. The estimate of the average displacement production rate by Si ion beam obtained using a relation similar to Eq. (1) gives $G_{Si} \approx 7.6 \times 10^{-4}$ dpa/s.

(c) Summary profiles of point defect generation. In order to estimate the total rates of damage production, it is important to take into account possible differences in the mode of defect creation by different beams. The contribution of any individual beam into the defect production rate can be written down as

$$G(z) = \zeta G_0 \varphi g(z), \tag{2}$$

where ζ is the cascade efficiency (a factor that accounts for the collective effects in intracascade annealing,[11,12] if relevant), φ the particle flux in the units of $1/cm^2/s$, G_0 the value of the point defect production in the peak, as predicted by SRIM code, and $g(z)$ a function that describes the depth variation of the damage profile predicted by SRIM. With such a definition of G_0, the profile function g is normalized so that it equals unity at the position of profile maximum. In the IVEM experiment, the values of G_0 are equal to 4.5×10^{-15} dpa/(ion/cm^2) for Co^+ beam and 5×10^{-23} dpa/(e^-/cm^2) for the 300-keV electron beam. For JANNuS conditions, the estimates of G_0 for Co^+ and Si^+ beams give 8.5×10^{-15} and 0.9×10^{-15} dpa/(ion/cm^2), respectively. No reliable values of the

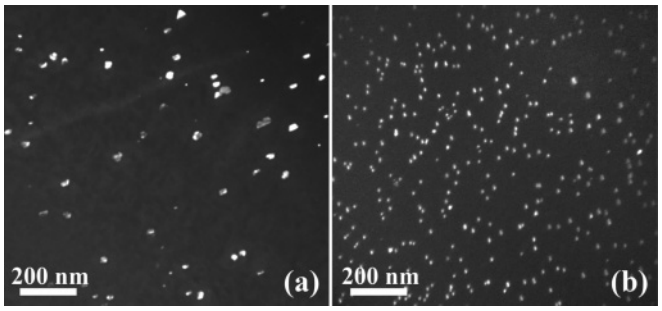

FIG. 9. B-type precipitates observed on $(110)_{CoSi2}//(114)_{Si}$ plane by means of a $g_{(111)}$ diffraction vector. (a) In zone 2 of Fig. 1, i.e. with Co implantation alone; (b) in zone 1 of Fig. 1, i.e. on a dual-beam area. The specimen thickness is similar in both areas.

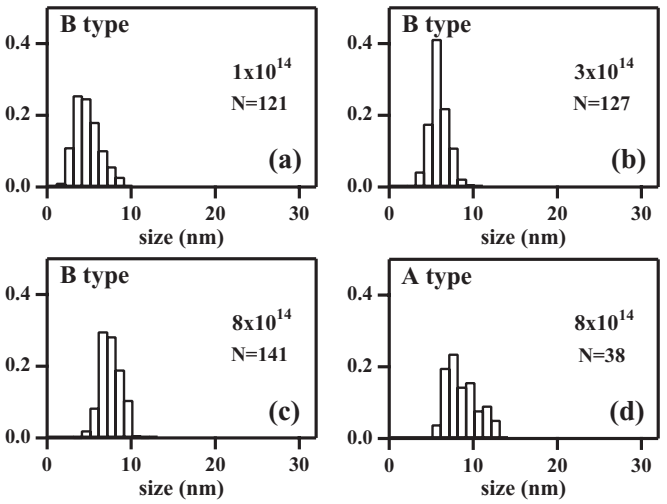

FIG. 10. (a)–(c) Size distributions of B-type $CoSi_2$ precipitates at different Co^+ fluences (Co/Si dual-beam experiment, JANNuS), as indicated in the legends (in ions/cm^2). The legends indicate also the total number N of precipitates used for histogram creation. (d) The A-type precipitate size distribution on the same area for the highest fluence only.

TABLE III. $CoSi_2$ precipitate number densities and mean sizes at different Co fluences for the JANNuS experiments.

		Saturated number density	Mean diameter (nm) at Co fluences of:		
	$CoSi_2$ type	(10^{10}/cm^2)	10^{14}/cm^2	3×10^{14}/cm^2	8×10^{14}/cm^2
Single Co beam	A	0.15			14
	B	2.9			15
Dual-beam Co + Si	A	0.5			9
	B	23	5	6	7.5

cascade efficiency factor for cascades in silicon are reported in the literature, but a reasonable estimate from molecular dynamics calculation (see Sec. IV B below) would be $\zeta = 0.2$.

The total defect production rates in both experiments can be calculated by summation of Eq. (2) for the relevant beam contributions. In particular, Fig. 12 shows the summary defect production profiles for JANNuS experimental conditions and for two combinations of experimental conditions of IVEM (ion and electron dominated regimes). The cascade efficiency value $\zeta = 0.2$ for all ion beams has been applied, whereas $\zeta = 1$ for the electron beam, which produces no collision cascades. The estimated peak value of damage production rates in JANNuS is 2×10^{-3} dpa/s, while for IVEM it is 1.3×10^{-3} and 2.9×10^{-3} dpa/s for ion and electron dominated regimes, respectively.

2. *The spatial distributions of freely migrating defects*

According to the estimates above, the rates of freely migrating defect production in our experiments is very high, but the evolution of the microstructural features (dislocation loops and precipitates) is determined by the instantaneous concentrations of vacancies and interstitials that are established as a balance between point defect production by implantation/irradiation and point defects annealing at the sample surfaces and internal sinks. TEM samples are very thin ($\leqslant$100–120 nm), while both vacancies and interstitials in silicon are very mobile.[13] At 650 °C, the freely migrating point defects should be very efficiently removed from the sample, so that even high defect production rates do not guarantee high concentrations of vacancies and interstitials in it.

In order to estimate the concentrations of freely migrating vacancies and interstitials that establish in the samples in our experimental conditions, we apply a mathematical model of the type commonly used for the analysis of dislocation loop growth in TEM conditions (e.g. Ref. 14). The model is described in detail in Appendix A. In brief, the point defect concentrations are found from the solution of diffusion equations that consider both the spatial variation of defect generation rate and the point defect loss to grain boundaries and internal sinks. The important internal point defect sinks in the TEM samples are impurity atoms and, after a certain implantation/irradiation dose, dislocation loops that are quickly formed after the irradiation onset.

In our experiments, the phosphorus doping level $\sim 6 \times 10^{12}$ P/cm^3 was too low to affect the point defect concentrations. The concentrations of oxygen and carbon atoms (which can capture, respectively, vacancies and interstitials[13]) could not be measured by the available equipment, but 10^{15} cm^{-3} seems a reasonable upper bound for our float-zone silicon samples.[15] The dislocation density, negligible in the nonimplanted samples, increases during implantation and can reach $\sim 2 \times 10^{11}$ cm^{-2} at the highest achieved Co ion fluence (see Table I). The estimates in Appendix A indicate that at the initial stages of implantation, when the dislocation sink strength is below $\sim 10^9$ cm^{-2}, the point defect loss is dominated by the surface absorption; while at higher dislocation sink strength, the role of surface absorption becomes relatively minor as compared to the loss to dislocation loops. Assuming the

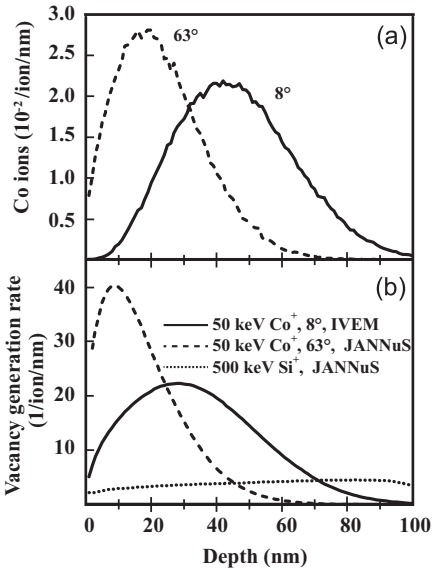

FIG. 11. (a) Depth distributions of 50-keV Co ions falling at inclination 8° and 63° to the sample surface and (b) vacancy generation rate profiles for Co and Si ion beams, as predicted by SRIM-2006 code.

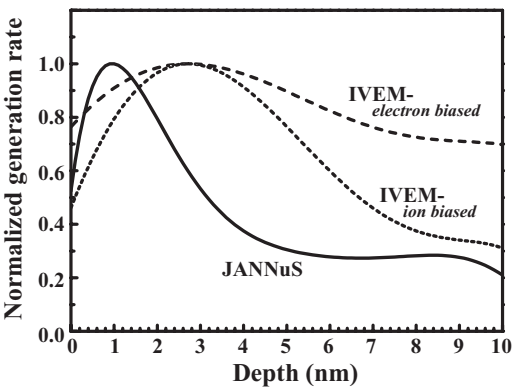

FIG. 12. Depth profile functions $g(z)$ for the IVEM (dash and dot curves for ion- and electron-biased regimes, respectively) and JANNuS (solid) experiments.

typical observed loop number density of ~2–5 × 10^{15} cm^{-3}, the transition from surface to dislocation-dominated regimes of point defect loss occurs when the average diameter of dislocation loops reaches ~1–2 nm.

As demonstrated in Appendix A, the concentrations $C_\alpha(z)$ of either interstitials ($\alpha = I$) or vacancies ($\alpha = V$) can be normalized as

$$C_\alpha(z) = C_{\alpha 0} c(z), \tag{3}$$

where c is the normalized concentration (the same for vacancies and interstitials) and

$$C_{\alpha 0} = \frac{\zeta G_0^{\mathrm{Co}} \varphi^{\mathrm{Co}} h}{D_\alpha},$$

where h is the specimen thickness and D_α the diffusion coefficient for α-type point defects. The superscripts indicate that the corresponding parameter is that for the Co beam in a considered experiment.

The calculated normalized depth distributions of point defects for our experiments are shown in Fig. 12. Each figure includes curves corresponding to different dislocation densities varying from the surface-dominant (early implantation stages) to dislocation-dominant (late implantation stages) regimes of point defect annihilation.

The factors $C_{\alpha 0}$ depend on both the implantation intensity and the point defect diffusion coefficients. The latter are estimated in Appendix B. For the interstitial diffusion coefficients, two possibilities are considered, where interstitials are faster or slower than vacancies. The resulting values of $C_{\alpha 0}$ and the maximum point defect concentrations, $C_{\alpha \max}$, are collected in Table IV. In spite of the high point defect generation rates in both of our experiments, the concentrations of freely migrating point defects in implanted samples remain at a very low level, with the peak concentration of interstitials remaining well below 10^{-8}–10^{-9}/atom.

3. *The secondary damage kinetics*

To sum up, let us discuss the observed microstructural evolution in terms of the estimates above.

(a) Dislocation loops in TEM specimens. As shown in the preceding section, in TEM specimens, a combination of powerful point defect sinks (sample surfaces) and the fast point defect diffusion leads to an overall low level of defect concentrations. One might expect that, in these conditions, no extended defects are produced. In agreement with that, no visible dislocation loops or voids are produced by the 300-keV electron beam (see Sec. III A 2), but during Co ion implantation into TEM samples, dislocation loops are a common feature (e.g. Ref. 4). In this section, we demonstrate that this effect cannot be explained considering solely the freely migrating defects.

TABLE IV. The concentration normalization factors $C_{\alpha 0}$ and the maximum point defect concentrations $C_{\alpha \max}$ (per atom) for the conditions of IVEM and JANNuS experiments.

	IVEM(electron-biased)	IVEM(ion-biased)	JANNuS
C_{V0}	4.46×10^{-12}	1.1×10^{-11}	2.3×10^{-11}
C_{I0}	5.9×10^{-13}	1.5×10^{-12}	3.7×10^{-12}
C_{I0}[a]	1.5×10^{-9}	4.6×10^{-9}	9.3×10^{-9}
$C_{V\max}$	4.9×10^{-13}	1.0×10^{-12}	1.2×10^{-12}
$C_{I\max}$	6.5×10^{-14}	1.3×10^{-13}	1.6×10^{-13}
$C_{I\max}$[a]	1.7×10^{-10}	5×10^{-10}	4.7×10^{-8}

[a]Assuming slow diffusion mode.

(i) First of all, let us consider a single-beam situation. The nucleation of point defect clusters from freely migrating defects can happen either via direct point defect collisions or through point defect capture at some nucleation centers, such as impurity atoms. In our case, neither mechanism looks plausible. The typical loop number densities in our experiments are 10^{15}–10^{16} cm^{-3} (see Table I). This excludes a possibility of loop nucleation on impurities because the impurity concentrations in our float-zone specimens are definitely lower. Loop nucleation by direct collision of freely migrating interstitials also seems improbable, in spite of the fact that at 650 °C, even the smallest interstitial clusters (di- and tri-interstitials) are stable against thermal dissociation[16] and, once formed, do not break. The steady-state number density of dislocation loops cannot exceed the steady-state monomer concentration prior to the onset of cluster nucleation. Table IV shows that steady-state interstitial concentrations comparable to the observed loop number density can be obtained assuming that interstitials are slow diffusers. Even not being completely impossible, such an assumption diverges from the generally accepted view that interstitials in silicon diffuse at least faster than vacancies.[17] Moreover, di-interstitials and, to a lesser extent, tri-interstitials in silicon are mobile[18,19] and, similar to mono-interstitials, are able to escape to sample surfaces. Our molecular dynamics simulations (to be reported in detail elsewhere) indicate that, only starting from 4–5 interstitials, the interstitial clusters are sufficiently immobile in order to be considered as nuclei of extended defects. The experimental measurements[20] also point out that the critical nucleus for the extended interstitial defects contains at least several interstitials. Even assuming the slow interstitial diffusion mode, the concentration of freely migrating interstitials remains too low to create a noticeable amount of at least tetra-interstitials through direct interstitial clustering.

(ii) Now, let us see what happens with dislocation loops when the ion and electron beams are applied at the same time. An addition of an electron beam increases the generation rates of freely migrating point defects. In terms of the classical nucleation theory, this should result in the increase of the loop number density, accompanied with the decrease of the loop sizes (at the same equivalent dose). What is observed is exactly the opposite; the loop number density is notably higher in the area outside the electron irradiated spot, whereas the loops are much bigger inside it. It looks like the electron beam continues to act in exactly the same way as in the case when it is applied alone; that is suppressing the dislocation loop nucleation.

(b) $CoSi_2$ nucleation. The dual beam experiments bear important messages for the better understanding of cobalt disilicide nucleation mechanisms. As mentioned earlier, cobalt implantation creates two types of $CoSi_2$ particles with pronouncedly different shapes. The relative shares of A- and B-type precipitates are sensitive to the experimental regimes. According to our earlier investigations,[4,5] A-type precipitates form via straightforward clustering of Co atoms, and their nucleation is limited mostly by the availability of Co interstitials. In contrast, the nucleation of B-type precipitates is triggered by Co capture on vacancies and small vacancy-type defects,

being sensitive to both the rate of Co supply and the efficiency of radiation damage production.

The detailed mechanism of B-type particle nucleation suggested in Refs. 4 and 5 considered cobalt atom interaction with monovacancies. The results of the IVEM experiment indicate that the account of only monovacancies as Co trapping sites may be insufficient. Indeed, the electron beam, especially at the highest beam intensity, significantly accelerates the monovacancy generation. The additional vacancies should promote the nucleation of B-type precipitates, without having a big effect on A-type, implying the overall decrease of the A-to-B particle number density ratio. In contrast, the electron beam weakly increases the precipitate number densities, either B- or A-type. Moreover, the most intensive electron beam promotes rather A-type precipitate formation. The increase of the relative share of A-type clusters is not spectacular, but statistically significant, having in mind that the cluster statistics inside and outside of the electron-irradiated spot are accumulated on the same sample.

The vacancy concentration level of 10^{11}–$10^{12}/\mathrm{cm}^3$, as estimated in Sec. III B 2, also looks too low to efficiently promote the nucleation of B-type particles. Already, after several microseconds of Co implantation, the concentration of implanted Co noticeably exceeds this level, and the direct collisions of cobalt atoms favoring the nucleation of A-type particles become much more frequent than Co atom collisions with vacancies. The fact that B-type nucleation dominates in our experimental conditions indicates that, in addition to monovacancies, some other efficient vacancy-type traps for Co with notably higher concentration should be considered.

The most evident candidates for such traps are very small vacancy clusters, like di- or trivacancies. In contrast to vacancies, already a divacancy moves in silicon relatively slow (with the migration energy of $\sim$1.2 eV),[21] while a trivacancy is practically immobile. Once formed, small vacancy clusters cannot move out of the specimen and thus are accumulated inside it. However, dealing with only the freely migrating vacancies, we meet exactly the same problem as that discussed in relation to dislocation loop nucleation. It remains unclear how to accumulate sufficient vacancy cluster concentrations in order to promote the observed number densities of B-type precipitates.

The combination of Co and Si ion beams in the JANNuS experiment also demonstrates something unexpected. The increased damage production decreases the A-to-B-type number density ratio, in line with the earlier model,[4,5] but the effect (nearly five times decreased as compared to the single Co beam) looks too strong for quite moderate enhancement of the overall point defect production by the secondary Si beam.

IV. MODELING OF DAMAGE KINETICS IN DUAL-BEAM IMPLANTATION CONDITIONS

A. Working hypothesis

The discussion in Sec. III B 2 evidences that the experimental observations cannot be fully explained without a detailed consideration of the defect production modes by different beams.

The fact that dislocation loops are nucleated by ions beams, which create multiple collision cascades, suggests that the nucleation of loops is somehow related to the cascades. In fact, the large body of available knowledge about collision cascades in different materials (see e.g. Refs. 22 and 23 for a general review on the subject) provides at least two suggestions of how the correlated defect production in collision cascades could promote a nucleation of point defect clusters. First of all, clusters can be leftovers of a local material redistribution during the formation stage of a cascade (displacement spike eventually followed by thermal spike). Although the general trend is that mostly vacancy-type clusters are left after the thermal spike cooling down, the infrequent events of interstitial cluster creation directly at the ballistic cascade stage are also reported, at least for some metals.[11,24] Second, a sufficiently energetic cascade produces noticeable amounts of defects in a localized volume of material affected by the cascade (cascade region). It takes some time for the freely mobile point defects in the cascade remnants to leave the cascade region and dissipate among the other defects in the volume of the sample. That is, for a certain time, the probability for mobile defect collisions between themselves and with the immobile clusters in the cascade region remains noticeably higher than in the bulk of the sample, where the average point defect concentrations are much lower. Even then, one can hardly expect the resulting interstitial clusters to contain more than several interstitials, but as discussed above, at this stage only, the nuclei for extended interstitial defects are to be created, and these nuclei are quite small (tetra-interstitials).

Taking into account the direct dislocation loop nucleation in collision cascades, the observed effects of the electron beam on the dislocation loop nucleation can be explained by invoking some basic results of the first-order transition theory (e.g. Refs. 25 and 26) as applied to dislocation loops. To start with, the direct in-cascade creation of loop nuclei does not guarantee that all the created loop nuclei ultimately survive and evolve into visible extended defects. The loop nuclei can be destroyed by radiation-produced vacancies and by thermal dissociation, though, at our working temperatures, the latter is probably not very efficient because the reported threshold for interstitial loop dissolution (1200 °C)[27] is well above the temperature of our experiments. The relative share of surviving loops is quite sensitive to the balance between the vacancies and interstitials in the sample volume. The quantitative measure for the balance is the ratio between the freely migrating point defects currents, $J_V = D_V C_V$ and $J_I = D_I C_I$. The lower is the ratio J_V/J_I, the higher is the number of surviving loop nuclei. Because a noticeable part of cascade-generated vacancies is usually retained in long-living and immobile vacancy clusters, the relation $J_V/J_I < 1$ usually holds for a cascade-producing irradiation. The switching on of an electron beam, which produces exactly equal numbers of vacancies and interstitials, inevitably shifts the ratio J_V/J_I closer to unity. The more intensive the electron beam, the more pronounced the shift, i.e. the smaller the share of surviving loop nuclei. This is exactly what we observe.

Finally, the cascade mode of damage production can explain the origins of large amounts of small vacancy clusters necessary for the nucleation of cobalt disilicide. Collision cascades in general are known to produce a certain share of the primary damage in the form of small vacancy clusters. When this share is high enough, the concentration of vacancy clusters can become sufficient for the creation of observed number

densities of disilicide precipitates. Indeed, let us consider the simplest situation when in addition to monovacancies, cascades produce a certain amount of divacancies with the generation rate of $0.5\varepsilon_{V2}G_{\mathrm{Co}}$, where the factor ε_{V2} indicates the share of the total vacancy production in the divacancy form. As a result of a continuous divacancy production, the steady-state divacancy concentration is established as a balance between divacancy creation and destruction. Due to the suppressed mobility of divacancies, their dominant destruction mode is thermal dissociation. Taking 1.8 eV for the divacancy binding energy,[28] the average thermal lifetime of divacancies at 650 °C can be estimated as $\tau_{V2} \approx 10\ \mu$s. Then the steady state divacancy concentration, C_{V2}, can be roughly estimated as

$$C_{V2} = 0.5\varepsilon_{V2}Gc_0\tau_{V2}.$$

Assuming that, say, 10% of the whole vacancy production is in the form of divacancies, and recalling the overall rates of damage creation in our experiments ($G_{\mathrm{Co}} \sim 10^{-3}$ dpa/s), we get $C_{V2} \sim 10^{-9}$; that is nearly three orders of magnitude higher than that of freely migrating vacancies and only an order of magnitude lower than the typical observed number densities of disilicide clusters. In fact, even this order-of-magnitude discrepancy can be eliminated, assuming that the dominant part of the vacancy-type damage in collision cascades consists of small vacancy clusters. Though the latter assumption might look exaggerated, in the case of silicon, it turns out to be quite close to reality (see Sec. IV B below).

Thinking back, the model of B-type cluster nucleation on the cascade-produced vacancy clusters gives a straightforward explanation of an earlier unresolved problem related to the interpretation of our earlier experimental findings.[4] In particular, there it was demonstrated that, at 650 °C, the saturation value for the disilicide precipitate number density, N_c, was directly proportional to the Co beam intensity, while the theoretical estimates based on the assumption of Co atom trapping on freely migrating vacancies predicted the square root dependence of N_c on the cobalt ion flux. However, when B-type disilicide nucleates on cascade debris, the number density of clusters is proportional simply to the amount of available nucleation sites (small vacancy clusters), which grows linearly with the ion flux.

To sum up this section, a detailed consideration of the defect production modes of different beams allows us to suggest a qualitative explanation for the effects observed in the current experiment. In the next section, we provide the modeling results in support of this interpretation.

B. Damage production in Si by collision cascades

The discussion in Sec. IV A relies on the generally known features of collision cascades, rather than on detailed information about cascades in silicon, but the available cascade calculations deal mostly with metals. While the qualitative trends of cascade behavior in different materials can be expected to be largely similar,[22] a quantitative extrapolation of metal-based simulation results to silicon is risky because cascades in covalent semiconductors manifest also serious differences from cascades in metals. The most important difference is that collision cascades in covalent semiconductors produce relatively big (of nanometer size range) amorphous zones, which are not observed in metals. The effect is well known from both the experimental studies[29–31] and molecular dynamic (MD) simulations (e.g. Refs. 32 and 33). At temperatures relevant to our experiments these amorphous zones eventually dissolve, but on the atomistically long time scales (minimum of nanoseconds[33–36]). This implies that the numbers and size distributions of defects ultimately produced in cascades are determined not only by the fast material heat up at the formation cascade stage, as is the case for metals, but also by the relatively slow amorphous zone dissolution kinetics. The outcome of this dissolution cannot be even approximately predicted from metal-based calculations.

The basic source of knowledge about the radiation damage production in collision cascades is currently molecular dynamics simulations. In spite of the fact that various aspects of radiation damage creation in silicon remain a long-lasting research topic, the damage produced by sufficiently energetic recoil atoms (>0.5 keV) is studied in a relatively limited number of papers.[22,32–35,37,38] Most of them address the damage created at the ballistic cascade stage and seldom continue beyond several tens of picoseconds. The long-term simulations aimed to clarify the detailed nature of the damage left after the dissolution of amorphous zones were undertaken rarely[33–35] and usually dealt with individual amorphous zones cut off of the initial simulation cells and held at elevated temperatures (>1000 °C) until dissolution. Alternatively, artificially created amorphous zones were annealed at high temperatures.[36] All these studies indicate that quite simple defects are left after the complete annealing of amorphous zones. However, the available data cannot be used to either support or discard the picture outlined in Sec. IV A.

Due to the lack of an appropriate database, we have performed an extensive molecular dynamics simulation of postballistic annealing of cascade damage. Here, we present the calculation results that are directly relevant for the topic of the paper; other data will be reported elsewhere.

1. Methodological aspects

Molecular dynamics simulations reported here were performed using the LAMMPS code.[39] Among several widely used silicon interatomic potentials, such as Stillinger–Weber, Tersoff or EDIP, the Tersoff potential (multicomponent version[40]) was preferred, mainly because our own experience and the reported results of Ref. 36 indicate that it reasonably reproduces the small defect clusters predicted by first-principles or tight-binding calculations.[16,41] In order to properly describe the strong repulsion at small interatomic distances (<0.8 Å), the Tersoff potential is smoothly connected (by a Fermi-like function, as implemented in LAMMPS) to the universal Ziegler–Biersack–Littmark potential.[9]

In this paper, we have calculated the damage produced by silicon recoils with the initial energies in the range of 0.5–5 keV. At each recoil energy, 8–10 cascades were simulated in order to get representative statistics. The choice of the energy range is determined by the fact that, below 0.5 keV, no real cascades are produced,[42,43] while at higher energies, there is a strong tendency for collision cascades to separate into spatially distinguished subcascades. In our

simulations, this trend starts already for 3-keV recoils and becomes quite pronounced at 5-keV recoil energy. At 10-keV recoil energy, the cascades are known to completely break into subcascades.[22] The defect production in subcascades is qualitatively the same as that produced by lower-energy recoils, so it makes little sense to model very energetic recoils directly. Moreover, according to SRIM-based calculations, for both Co and Si ions, the relative number of cascade-producing primary recoils (that is those with the energy above ∼0.3 keV) sharply falls with the increase of the recoil energy (see Fig. 13). For the 50-keV Co ion beam, ∼90% of the recoils with the energy in the range of 0.25–5 keV are primary knock-on atoms, and only the remaining 10% are able to create subcascades. For 500-keV Si ions, the relative part of primary recoils in the same energy range is also significant (∼50%), but the share of high-energy recoils is nonnegligible, and the contribution to damage from subcascades caused by secondary recoils must be properly taken into account in order to quantify the number of interstitials and vacancies generated by the Si beam.

The used simulation cells had cubic shapes and periodic boundary conditions along all the coordinate axes. The cell edge lengths were $24a$ (accommodating $\sim 1.1 \times 10^5$ atoms per cell) for recoil energies $\leqslant$3 keV and $36a$ ($\sim 3.8 \times 10^5$ atoms) for 5-keV recoils, where $a = 5.432$ Å is the silicon lattice parameter for the Tersoff potential.

The simulation temperature was selected equal to 1000 K; that is somewhat higher than the experimental temperature (923 K). This is a standard practice for the Tersoff potential, which overestimates the crystal melting temperature and thus requires an upward temperature shift to avoid decelerated kinetics (the value of the shift in our case was estimated using the relation suggested in Ref. 44). The cascades were initiated in a lattice preliminary equilibrated at this temperature. To launch a cascade, the momentum of one atom (recoil) was replaced with that corresponding to the desired recoil energy and oriented randomly in space. In order to acquire statistics, 8–10 initial orientations of recoil momenta were applied at each energy. The time step for the MD simulation was 0.1 fs for the first 1 or 2 picoseconds (depending on PKA energy) and 1 fs later on. The annealing at 1000 K

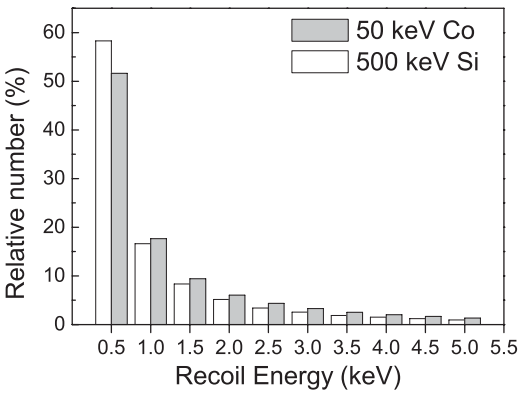

FIG. 13. The energy distribution of primary recoils in the energy range 0.25–5 keV for Co^+ and Si^+ beams in the conditions of the JANNuS experiment. The total amount of recoils in the considered energy range is taken equal to 100% for each beam. Calculations were done with the SRIM-2006 code.

continued until all the amorphous zones were completely annealed, which meant simulation times of 1–10 ns, depending on the recoil energy and the particular cascade. After the termination of the amorphous zone annealing, the remaining point defects and defect clusters were typically located quite near to each other, so that a further annealing of cascade remnants remained highly probable. However, at 1000 K, the recombination of closely lying defects takes too much time to simulate. In order to accelerate the recombination kinetics, the temperature was additionally increased to 1300 K and the annealing continued until all mobile defects (vacancies, interstitials and di-interstitials) were located sufficiently far (at least 1 nm) from each other and from the immobile defects. The temperature was maintained during simulation using the Berendsen thermostat.

In order to quantify the numbers of defects remaining in the cascade regions after the annealing, the final configurations were postprocessed using a procedure based on the so-called Lindemann sphere approach. In this approach, the positions of all atoms in the simulation cell are compared to the ideal silicon lattice. The atoms that fall within small spherical regions centered on the lattice sites are considered to be regular lattice atoms, while the atoms outside these spheres are marked as displaced. The embedding spheres that contain no atoms are marked as vacant sites (which are not necessarily vacancies in the usual sense). The radius of spheres should be selected so that it remains smaller than the typical distance between atoms in known interstitial defects. In practice, the radius of 0.7–0.8 Å gives good results; the value of 0.7 Å is suggested also by other authors using the same approach.[36] In addition, the postprocessing includes several features allowing a reliable identification of point defects and defects clusters, rather than simply a calculation of the number of displaced atoms. Special measures are taken to eliminate spurious contributions to the calculated point defect numbers from the thermal motion of atoms; these contributions are negligible at 1000 K but are of serious concern at 1300 K. As a rule, the postprocessing allows us to eliminate the thermal motion contributions on the fly, but the configuration snapshot cooling down to 0 K was additionally applied to eliminate the uncertainties when a precise quantitative information was required. A detailed description of the postprocessing technique is given elsewhere.[45]

A typical postprocessing result is shown in Fig. 14, which shows a representative example of cascade remnants after the dissolution of amorphous zones and the elimination of closely lying mobile defects. Individual defects can be identified as small clusters of intermixed displaced atoms and vacant sites. The assignment of a particular defect to a cluster involves the use of cluster rank, which is the difference between the numbers of displaced atoms and vacant sites in the cluster. Thus, all clusters with rank 1 are considered as mono-interstitials, those with rank 2 as di-interstitials, etc. Correspondingly, vacancy-type clusters have negative ranks (−1 for monovacancies, etc.). As can be noticed in the figure, even monodefects are often represented by clusters consisting of several displaced atoms and vacant sites. Moreover, defects of the same rank can exist in clusters of different shape, which is the manifestation of the multiconfigurational nature of basic point defects in silicon.[46]

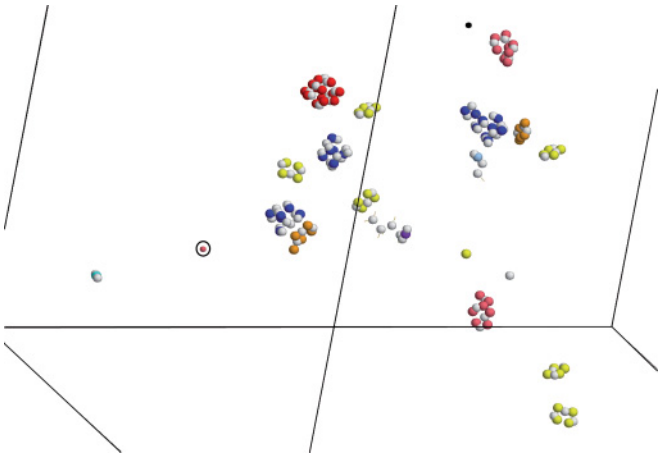

FIG. 14. (Color online) An example of point defect and defect cluster distribution in the cascade region after 1.5-ns-long annealing at 1000 K and a subsequent annealing for 1 ns at 1300 K. The initial recoil energy is 3 keV. Only displaced atoms (colored) and vacant sites (white) are shown. Different colors of displaced atoms correspond to different cluster ranks. The initial and final positions of the recoil are respectively indicated by a small (in color, pink) dot bounded by a black circle and a small black dot.

2. Simulation results

The MD simulations have demonstrated an unexpectedly strong asymmetry in the levels of clusterization of vacancies and interstitials surviving after the recrystallization of in-cascade amorphous zones. As can be seen in Fig. 15, the majority of vacancies is captured in the relatively or completely immobile vacancy clusters, whereas the interstitials are generated mostly as monodefects.

Most often, clusters consisting of two and three vacancies are formed, but bigger clusters (up to 12 vacancies) are also observed at higher recoil energies. However, the bigger the vacancy cluster size, the less frequently is it observed and the higher is the threshold recoil energy for its creation. The analysis of the cascade annealing kinetics evidences that the vacancy clusters bigger than trivacancies are the remnants of dissolved amorphous zones. The biggest observed vacancy clusters remain from exclusively big amorphous zones produced rarely by high-energy recoils.

The heavy suppression of mobile monovacancy generation in cascades can be a possible reason why one does not observe

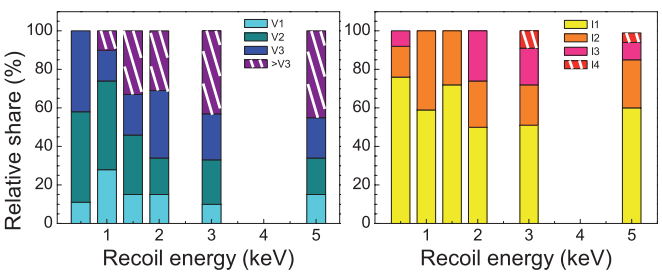

FIG. 15. (Color online) The partitioning of vacancies (left) and interstitials (right) between clusters of different sizes (as indicated in the legends) as a function of the initial recoil energy. The relative shares are averages over 8–10 cascades.

big vacancy clusters (voids) in ion-implanted silicon, whereas interstitial clusters nucleate even in such an unfavorable situation as the high-temperature implantation into TEM samples. Indeed, in spite of a relative abundance of void nuclei produced in cascades, only ∼10–15% of all created vacancies are able to leave cascade regions and contribute to vacancy cluster growth somewhere in the sample bulk.

In contrast to vacancy clusters, the formation of interstitial clusters bigger than a di-interstitial is not straightforward, even though overall possible. First of all, no formation of such interstitial clusters directly at the ballistic stage of a cascade was observed. Neither do they form as a result of amorphous zone dissolution. The main mechanism of tri- and tetra-interstitial nucleation is the classical agglomeration of freely migrating interstitials. The latter requires that the recoil energy is high enough to produce a sufficiently large number of interstitials. In our simulations, tri-interstitials are regularly observed starting from the PKA energy of 2 keV and tetra-interstitials from 3 keV, see Fig. 15. The fact that the majority of excess vacancies is immobilized in clusters and is unable to counteract the nucleation of small interstitial clusters largely simplifies the interstitial clusterization.

Finally, the molecular dynamic calculations allow us to estimate the cascade efficiency parameter, which was used in Sec. III B. By definition, the cascade efficiency is introduced as a correction coefficient in the equation relating the real number N of point defects produced in a cascade created by a recoil with the initial energy E and the value N_{BCA} predicted by calculations in the binary collisions approximation (BCA). Taking for the latter the commonly used Norgett–Robinson–Torrens (NRT) equation,[47] this relation can be written down as

$$N_{\mathrm{BCA}} = \zeta \frac{E}{2E_d}, \tag{4}$$

where E_d is the threshold energy for an impact atom displacement, and the factor ζ (∼0.8 for NRT-standard) accounts for the inelastic energy losses accompanying the cascade development at the ballistic stage. In spite of its

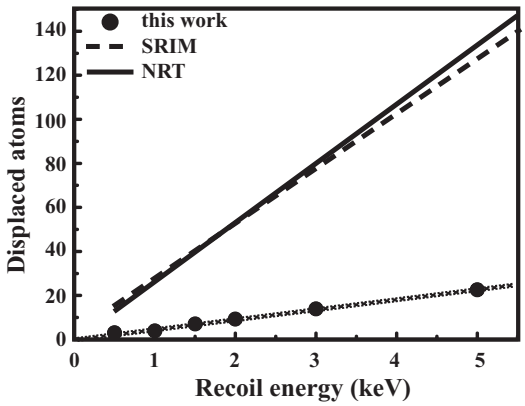

FIG. 16. The total calculated numbers of point defects (interstitials or vacancies) as a function of the recoil initial energies. The points at each energy are averages over 8–10 cascades. Calculation results are given by round points; the dash line is the least squares fit in the recoil energy range of 1–5 keV. For comparison, the predictions of Eq. (4) and direct SRIM calculations in the full cascade mode are shown with thicker solid and dash lines, respectively.

simplicity, Eq. (4) gives a very close approximation of the actual number of displacements predicted by, for example the SRIM code,[9] provided the same value of E_d is selected, Fig. 16. The proper value of the displacement threshold energy is not exactly known; different literature estimates fall within the range of 10–25 eV (for the detailed discussion of the problems of displacement threshold determination and the review of available calculations, refer to Refs. 48 and 49). To be specific, in Fig. 16 and in the discussion below, we use the standard reference value of 15 eV, as suggested by SRIM.

After the long-term annealing, the cascade remnants include no amorphous zones, making it possible to estimate the resulting damage directly in terms of the numbers of residual point defects. The total numbers of point defects (either vacancies or interstitials), including both monodefects and defects captured in clusters, are shown in Fig. 16 as a function of the initial recoil energy. It can be seen that the dependence is linear, but the slope is much lower than that predicted by either SRIM or Eq. (4). The MD and BCA results can be aligned, however, assuming the cascade efficiency $\zeta \approx 0.2$.

Summing up, our MD simulations confirm all assumptions used in Sec. IV A in order to rationalize the experimental observations. As assumed, small vacancy clusters are abundantly supplied with cascades initiated by recoils in the whole studied energy range, providing a possibility for the efficient trapping of freely migrating Co atoms. The nucleation of immobile small interstitial clusters is also demonstrated. Even though the small interstitial cluster creation is notably less efficient than for vacancy clusters and requires higher recoil energies, the overall generation rate of immobile nuclei of extended defects is sufficient to accumulate the observed loop number densities within the experiment durations. Finally, the production efficiency of freely migrating interstitials and vacancies is strongly biased in favor of interstitials, as is required to explain the effects of electron irradiation on the dislocation loop nucleation.

V. CONCLUSIONS

(1) In both dual-beam experiments, the addition of a second beam to the primary Co ion beam resulted in synergistic action that cannot be explained in terms of proportional intensification of primary damage production; the particular nature of these effects was completely different for the cases of electron and Si ion secondary beams. Additional damage in the form of Frenkel pairs, provided by fast electron irradiation, affected strongly the dislocation loop kinetics, but only weakly that of disilicide precipitation. The combination of Co and Si ion beams with nearly the same overall primary damage generation rate drastically increased the number density of thermodynamically unstable B-type $CoSi_2$ precipitates, as compared to the Co beam alone. The kinetics of other microstructural components (dislocation loops and A-type $CoSi_2$ precipitates) relatively weakly reacted to the moderate modification of primary damage production by Si beam.

(2) The analysis of the experimental results strongly suggests that both the dislocation loop nucleation and B-type disilicide precipitation during high-temperature *in situ* Co implantation are closely related to collision cascades produced by Co ions. In particular, the direct nucleation of dislocation loops in collision cascades could provide a reasonable explanation of the effects of electron irradiation on dislocation loop nucleation in TEM samples. The effects of both electron and silicon ion irradiation on the disilicide precipitation kinetics indicate that B-type $CoSi_2$ precipitates can nucleate on small vacancy clusters remaining after the annealing of collision cascades and not only on freely migrating vacancies, as we suggested earlier.

(3) In order to justify the assumptions about the detailed picture of damage creation by collision cascades, a systematic molecular dynamic simulation of the long-term annealing of cascade remnants created by energetic silicon recoils in the energy range of 0.5–5 keV has been undertaken. These simulations confirmed the main features of cascade damage production necessary to explain our observations, including a possibility of direct creation of both interstitial and vacancy small clusters in the cascade regions. A strong asymmetry in the clustering level of interstitial and vacancy defects remaining after the complete annealing of amorphous zones and subsequent recombination of closely lying mobile defects was observed: the majority of vacancies was captured in the relatively or completely immobile vacancy clusters, whereas the interstitials were generated mostly as monodefects. The overall number of surviving interstitials and vacancies was found to be roughly 20% of that expected from calculations in the binary collisions approximation.

ACKNOWLEDGMENTS

We are grateful to the JANNuS-Orsay team for ion beam supplies. We want to especially thank P. Baldo at IVEM, without whom no online experiment would be possible. The work was supported in part by a bilateral French-US collaboration program between CNRS and Argonne National Laboratory (2006-2008) and in part by the Grant No. 10-08-90041 from the Russian Basic Research Foundation. V.A.B. is deeply thankful to CSNSM for funding his research stays in France.

APPENDIX A: SPATIAL DISTRIBUTION OF FREELY MIGRATION VACANCIES AND INTERSTITIALS IN TEM SAMPLES

To a good approximation, the TEM sample can be treated as a thin foil irradiated with fast particles that produce inside the sample a damage with the depth-dependent generation rate $G(z)$, where z is the depth coordinate (normal to the sample surface). Because the foil thickness is notably less than the beam-covered area, we can consider the variation of the point defect concentrations as a function of z only.

In formulating the diffusion equation for point defects in TEM samples, two simplifications can be made. First of all, due to the high mobility of point defects, the spatial distributions of both vacancies and interstitials are assumed to quickly accommodate to the instantaneous sink distribution, so that on the time scale of sink density variation, the point defect profiles are quasisteady state (the adiabatic approximation). Second, the recombination between freely migrating interstitials and vacancies is neglected. As a result, the concentration profiles of interstitials and vacancies across the sample depth are

independent of each other, and the discussion below is applicable to either type of point defects.

The depth-dependent concentration of freely migrating point defects, C (z), is obtained from the solution of a one-dimensional steady-state diffusion equation, namely

$$G(z) + D\frac{d^2C}{dz^2} - k^2DC = 0, \tag{A1}$$

where D is the point defect diffusion coefficient and k^2 is the rate of point defect capture by internal sinks. At the free sample surfaces ($z = 0$ and $z = h$, where h is the sample thickness), C is assumed to vanish. Applying Eq. (3), an equation for the normalized concentration $c(z)$ is obtained in the form

$$\frac{d^2c}{d\tilde{z}^2} - k^2h^2c = -g_e(z), \tag{A2}$$

where $\tilde{z} = z/h$, g_e is the weighted average of contributions from individual beams,

$$g_e(z) = g_1(z) + \frac{\zeta_2 G_{02}\varphi_2}{\zeta_1 G_{01}\varphi_1} g_2(z),$$

and the profile functions g_1 and g_2 for the primary (cobalt) and secondary beam are as defined in Eq. (2). In order to get an analytical solution of Eq. (A2), the summary profile function is fitted by a polynomial,

$$g_e(z) = \sum_{m=0}^{M} \gamma_m \tilde{z}^m, \tag{A3}$$

where M and γ_0 to γ_M are fitting parameters.

The sink strength in our experiments can be written down as a sum of contributions from dislocation loops and, possibly, contaminating impurity atoms capable to capture the relevant point defects,

$$k^2 = Z_L N_L d_L + Z_c a^{-2} C_c,$$

where a is the lattice parameter, N_L and d_L the number density and the average size of dislocation loops, C_c the impurity concentration, Z_L and Z_c geometrical factors (typically $\sim$10) that take into account the capture efficiency of corresponding sinks. In the calculations, a constant value of $C_c = 10^{15}$ cm^{-3} was assumed. On the other hand, the dislocation density varied in our experiment in quite broad limits, from practically zero before implantation to $\sim$(0.5–2) $\times$ 10^{11} cm^{-2} at the highest achieved implantation fluences.

The solution of Eqs. (A2) and (A3) subject to the vanishing boundary conditions is

$$c(z) = \frac{1}{(kh)^2} \sum_{m=0}^{M} \frac{\gamma_m}{k^m} \left[P_m(kh) \frac{\sinh(kh\tilde{z})}{\sinh(kh)} - P_m(kh\tilde{z}) \right],$$

where the functions P_m are defined by recursive relations:

$$P_0(x) = \cosh x - 1, \qquad P_1(x) = \sinh x - x,$$

and

$$P_m(x) = -x^m + m(m-1)P_{m-2}(x) \quad \text{for} \quad m \geqslant 2.$$

The resulting point defect profiles for our experiments at different values of k^2 are shown in Fig. 17.

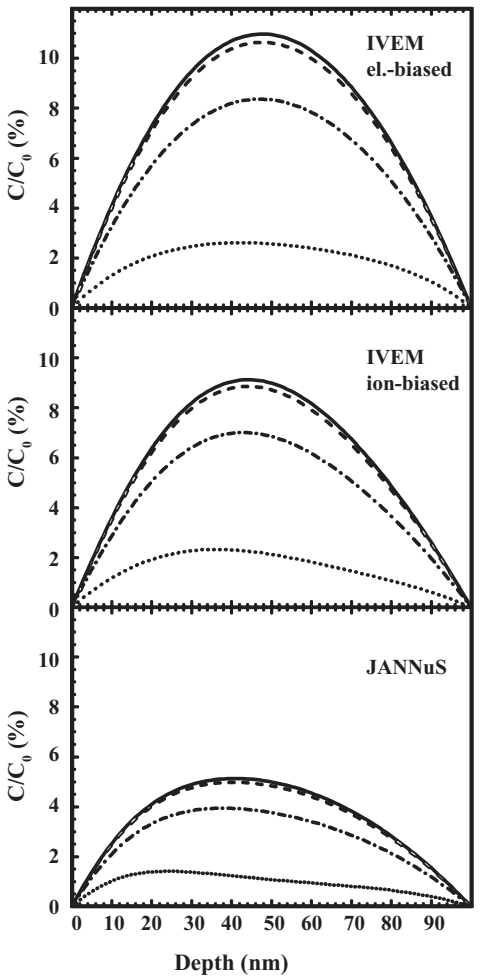

FIG. 17. The normalized point defect depth profiles, $C(z)/C_0$, for the experimental conditions of the IVEM and JANNuS experiments (as indicated in panel legends). Each plot includes curves for the impurity absorption dominated regime (any dislocation density ρ_d below $\sim 2 \times 10^8$ cm^{-2}), intermediate dislocation densities ($\rho_d = 10^9$ and 10^{10} cm^{-2}), and the dislocation absorption dominated regime ($\rho_d = 10^{11}$ cm^{-2}), shown as solid, dash, dash/dot, and dot lines, respectively.

Having the explicit relation for point defect spatial profile, one can determine the efficiency of point defect loss at the sample surfaces, k_S^2 :

$$k_S^2 = \frac{1}{h^2\langle c\rangle} \left(\left.\frac{dc}{d\tilde{z}}\right|_{\tilde{z}=0} - \left.\frac{dc}{d\tilde{z}}\right|_{\tilde{z}=1} \right),$$

where $\langle c\rangle$ is the average point defect concentration in the sample. As can be easily seen, the surface sink strength is sensitive to the particular bulk sink strength k^2. A straightforward calculation of k_S^2 as a function of k^2 in the range of 0 to 10^{11} cm^{-2} demonstrates that the point defect loss is controlled by surfaces only until the bulk sink strength remains below a certain critical value ($\sim$1.1 $\times$ 10^9 and $\sim$1.5 $\times$ 10^9 cm^{-2} for IVEM and JANNuS experiments, respectively). At higher values of k^2, the created point defects annihilate mostly at internal sinks.

APPENDIX B: INTERSTITIAL AND VACANCY DIFFUSION COEFFICIENTS IN SILICON

The diffusion coefficients for vacancies and interstitials can be estimated from the relation

$$D = D_0 \exp(-E_m/k_B T),$$

where D_0 is the pre-exponential factor, E_m the point defect migration barrier, k_B the Boltzmann constant, and T the absolute temperature. The prefactors are not well known experimentally for either vacancies or interstitials, but as an order-of-magnitude estimate, one can set $D_0 \approx 1$ cm^2/s. The vacancy migration energy for an intrinsic silicon is usually assumed to be $E_{mV} = 0.32$ eV,[13] which gives $D_V \approx 0.02$ cm^2/s at 650 °C. For interstitials, no experimental value of the migration barrier is available, though indirect evidence indicates that it must be very low (e.g. Ref. 17). The first-principles study for the equilibrium interstitial configuration (a split ⟨110⟩ dumbbell) suggests the migration barrier of $E_{mI} = 0.15$ eV.[50] With this migration energy, the interstitial diffusion coefficient at 650 °C is $D_I \approx 0.15$ cm^2/s. However, as evidenced by molecular dynamics studies,[44] a moving interstitial can spend a noticeable part of its lifetime in an immobile state (the so-called extended dumbbell configuration).[51] According to Ref. 44, the effective interstitial diffusion coefficient in this case remains Arrhenian, but the apparent migration energy noticeably increases (up to $E_{mI} = 0.77$ eV for the Tersoff potential used there). Taking the estimate of Ref. 44 at its face value, the slow diffusion of interstitials would be described by $D_I \approx 6 \times 10^{-5}$ cm^2/s.

[1] S. Mantl, Mater. Sci. Rep. **8**, 1 (1992).
[2] C. W. T. Bulle-Lieuwma, Ph. D. Thesis, Utrecht University, 1991.
[3] M. O. Ruault, F. Fortuna, H. Bernas, J. Chaumont, O. Kaïtasov, and V. A. Borodin, J. Mater. Res. **20**, 1758 (2005).
[4] M. O. Ruault, F. Fortuna, V. A. Borodin, M. G. Ganchenkova, and M. A. Kirk, J. Appl. Phys. **104**, 033527 (2008).
[5] V. A. Borodin, M. O. Ruault, M. G. Ganchenkova, and F. Fortuna, Sol. St. Phenom. **108-109**, 133 (2005).
[6] C. W. Allen, L. L. Funk, and E. A. Ryan, Mat. Res. Soc. Symp. **396**, 641 (1996); also [http://www.msd.anl.gov/groups/ht/].
[7] Y. Serruys, P. Trocellier, S. Miro, E. Bordas, M. O. Ruault, O. Kaïtasov, S. Henry, O. Leseigneur, Th. Bonnaillie, S. Pellegrino, S. Vaubaillon, and D. Uriot, J. Nucl. Mater. **386-388**, 967 (2009); also [http://jannus.in2p3.fr/].
[8] E. Oliviero, Ph. D. Thesis, University of Poitiers, 1998.
[9] J. P. Biersack and J. F. Ziegler, *The Stopping and Ranges of Ions in Solids* (Lulu Press Co., Morrisville, NC, 2008); see also [http://www.srim.org] for code description.
[10] O. S. Oen, Cross-sections for atomic displacements in solids by fast electrons, *ORNL Report TM-4897* (Oak Ridge National Laboratory, Oak Ridge, 1973).
[11] R. S. Averback, R. Benedek, and K. L. Merkle, J. Nucl. Mater. **69-70**, 786 (1978).
[12] P. Jung, J. Nucl. Mater. **117**, 70 (1983).
[13] G. D. Watkins, in *Deep Centers in Semiconductors*, edited by S. T. Pantelides (Gordon and Breach, New York, 1986), p. 147.
[14] K. M. Miller, S. B. Fisher, and R. J. White, J. Nucl. Mater. **110**, 265 (1982).
[15] A. Borghesi, B. Pivac, A. Sassella, and A. Stella, J. Appl. Phys. **77**, 4169 (1995).
[16] D. A. Richie, J. Kim, S. A. Barr, K. R. A. Hazzard, R. Hennig, and J. W. Wilkins, Phys. Rev. Lett. **92**, 045501 (2004).
[17] G. D. Watkins, Mat. Sci. Semicond. Proc. **3**, 227 (2000).
[18] S. K. Estreicher, M. Gharaibeh, P. A. Fedders, and P. Ordejon, Phys. Rev. Lett. **86**, 1247 (2001).
[19] M. Posselt, F. Gao, and D. Zwicker, Phys. Rev. B **71**, 245202 (2005).
[20] F. Schiettekatte, S. Roorda, R. Poirier, M. O. Fortin, S. Chazal, and R. Héliou, Appl. Phys. Lett. **77**, 4322 (2000).
[21] M. G. Ganchenkova, S. Nicolaysen, V. A. Borodin, E. Halvorsen, and R. M. Nieminen, Mat. Sci. Eng. B **134**, 244 (2006).
[22] K. Nordlund, M. Ghaly, R. S. Averback, M. Caturla, T. Diaz de la Rubia, and J. Tarus, Phys. Rev. B **57**, 7556 (1998).
[23] D. J. Bacon, Yu. N. Osetsky, R. Stoller, and R. E. Voskoboinikov, J. Nucl. Mater. **323**, 152 (2003).
[24] A. J. E. Foreman, W. J. Phythian, and C. A. English, Phil. Mag. A **66**, 671 (1992).
[25] J. L. Katz and H. Wiedersich, J. Chem. Phys. **55**, 1414 (1971).
[26] K. C. Russell, Acta Metall. **19**, 753 (1971).
[27] M. Servidori, I. Vecchi, E. Olzi, and G. Turisini, J. Mater. Sci. **17**, 301 (1982).
[28] M. G. Ganchenkova, V. A. Borodin, and R. M. Nieminen, Nucl. Instr. Meth Phys. Res. B **228**, 218 (2005).
[29] M. O. Ruault, J. Chaumont, J. M. Penisson, and A. Bourret, Phil. Mag A **50**, 667 (1984).
[30] I. Jenčič, M. W. Bench, I. M. Robertson, and M. A. Kirk, J. Appl. Phys. **78**, 974 (1995).
[31] S. E. Donnelly, R. C. Birtcher, V. M. Vishnyakov, and G. Carter, Appl. Phys. Lett. **82**, 1860 (2003).
[32] M. J. Caturla, T. Diaz de la Rubia, and G. H. Gilmer, Nucl. Instr. Meth. B, **106**, 1 (1995).
[33] M. J. Caturla, T. Diaz de la Rubia, L. A. Marques, and G. H. Gilmer, Phys. Rev. B **54**, 16683 (1996).
[34] T. Diaz de la Rubia and G. H. Gilmer, Phys. Rev. Lett. **74**, 2507 (1995).
[35] G. H. Gilmer, T. Diaz de la Rubia, D. M. Stock, and M. Jaraız, Nucl. Instr. and Meth. B **102**, 247 (1995).
[36] L. A. Marques, L. Pelaz, P. Lopez, I. Santos, and M. Aboy, Phys. Rev. B **76**, 153201 (2007).
[37] M. Posselt, Mat. Sci. Semicond. Proc. **3**, 317 (2000).
[38] S. M. Foiles, Nucl. Instr. and Meth. Phys. Res. B **255**, 101 (2007).
[39] S. Plimpton, J. Comp. Phys. **117**, 1 (1995) [http://lampps.sandia.gov].
[40] J. Tersoff, Phys. Rev. B **39**, 5566 (1989).
[41] N. Arai, S. Takeda, and M. Kohyama, Phys. Rev. Lett. **78**, 4265 (1997).
[42] G. Otto, G. Hobler, and K. Gärtner, Nucl. Instr. Meth. Phys. Res. B **202**, 114 (2003).

[43]M. J. Beck, R. Hatcher, R. D. Schrimpf, D. M. Fleetwood, and S. T. Pantelides, IEEE Trans. Nucl. Sci. **54**, 1906 (2007).
[44]L. A. Marques, L. Pelaz, P. Castrillo, and J. Barbolla, Phys. Rev. B **71**, 085204 (2005).
[45]V. A. Borodin, to be published in Nucl. Instr. Meth. Phys. Res. B (2011).
[46]M. G. Ganchenkova, L. E. Oikkonen, V. A. Borodin, S. Nicolaysen, and R. M. Nieminen, Mat. Sci. Eng. B **159-160**, 107 (2009).
[47]M. J. Norgett, M. T. Robinson, and I. M. Torrens, Nucl. Eng. Des. **33**, 50 (1975).
[48]M. Mazzarolo, L. Colombo, G. Lulli, and E. Albertazzi, Phys. Rev. B **63**, 195207 (2001).
[49]E. Holmstrom, A. Kuronen, and K. Nordlund, Phys. Rev. B **78**, 045202 (2008).
[50]W. C. Lee, S. G. Lee, and K. J. Chang, J. Phys. Condens. Matter **10**, 995 (1998).
[51]H. R. Schober, Phys. Rev. B **39**, 13013 (1989).